A Plasmonic Supramolecular Nanohybrid as a Contrast Agent for Site-Selective Computed Tomography Imaging of Tumor

Anivind Kaur Bindra, Sivaramapanicker Sreejith, Rajendra Prasad, Mahadeo Gorain, Rijil Thomas, Deblin Jana, Mui Hoon Nai, Dongdong Wang, Abhimanyu Tharayil, Gopal C. Kundu, Rohit Srivastava, Sabu Thomas, Chwee Teck Lim,* Yanli Zhao**

Dr. A. K. Bindra, Dr. D. Jana, Dr. D. Wang, Prof. Y. L. Zhao

Division of Chemistry and Biological Chemistry, School of Physical and Mathematical Sciences, Nanyang Technological University, 21 Nanyang Link, 637371, Singapore. Email: zhaoyanli@ntu.edu.sg

Dr. S. Sreejith, Prof. C. T. Lim

Institute for Health Innovation & Technology (iHealthtech), National University of Singapore, 14 Medical Drive, 117599, Singapore. Email: sreejith.siva@gmail.com, ctlim@nus.edu.sg

R. Prasad, R. Srivastava

Department of Biosciences and Bioengineering, Indian Institute of Technology-Bombay, Mumbai, 400076, India.

M. Gorain, G. C. Kundu

Laboratory of Tumor Biology, Angiogenesis and Nanomedicine Research, National Center for Cell Science, 411007, Pune, India.

R. Thomas

School of Electrical and Electronic Engineering, Nanyang Technological University, 50 Nanyang Avenue, 639798, Singapore.

M. H. Nai, Prof. C. T. Lim

Department of Biomedical Engineering, National University of Singapore, 117583, Singapore.

Dr. S. Sreejith, A. Tharayil, S. Thomas

School of Energy Materials, Mahatma Gandhi University, Kerala, 686560, India.

G. C. Kundu

School of Biotechnology and Kalinga Institute of Medical Sciences (KIMS), KIIT Deemed to be University, Bhubaneswar, 751024, India.

A. K. Bindra, S. Sreejith, and R. Prasad contributed equally to this work.

Abstract: Design of organic-inorganic hybrids by anchoring of plasmonic materials such as gold nanoparticles (AuNPs) on self-assembled organic substrates is useful but challenging. Herein, *in situ* anchoring of plasmonic nanoparticles on the surface of a designed spherical assembly *via* Au-S bond formation is presented. First, a thiol tailed pyrene derivative (**2**) undergoes solvent dependent self-assembly, transforming into organic spherical aggregate (**2**$_{agg}$). The thiol (-SH) rich surface of the organic assembly allows cumulative anchoring of AuNPs on the surface to form an organic-inorganic hybrid (**Au@2**$_{agg}$). Further coating of biocompatible polyethylene glycol (PEG) leads to the construction of the final multicomponent system (**PEG-Au@2**$_{agg}$) exhibiting morphological and spectroscopic features. The potential of **PEG-Au@2**$_{agg}$ as a bioprobe and a contrast agent was investigated by X-ray computed tomography (CT) experiments *in vivo*. High X-ray attenuation of directly anchored AuNP clusters on the surface of this supramolecular nanohybrids enhances the X-ray CT contrast and allows tracing of site-selective accumulation in mouse 4T1 breast tumor. Thus, this approach of designing organic-inorganic nanohybrids paves the way for developing future intelligent multifunctional nanosystems capable of cancer detection and imaging.

Keywords: bioimaging, mammary carcinoma, organic-plasmonic hybrid, self-assembly, X-ray computed tomography

Introduction

A precise control over the topological features associated with nanoscale structures formed *via* supramolecular assembly of organic and inorganic units remains challenging.[1-3] Engineering of extended noncovalent interactions between organic segments is important in limiting the formation of higher ordered assemblies and random aggregates.[4,5] For the design of functional hybrid materials involving second order assembly of inorganic component, directional interactions (*e.g.*, π-π stacking and solvent interactions) are preferred, since they allow better control over the self-assembly of organic segments as the base unit.[6-8] In this context, small organic molecules are ideal choices as soft templates owing to their easy availability, tunable synthesis, being inexpensive, and possessing various active sites for the self-assembly *via* noncovalent interactions.[9,10] The presence of self-assembling units connected covalently with specific functional moieties capable of anchoring inorganic units such as plasmonic nanomaterials leads to meticulous arrangement of these inorganic particles with the concomitant formation of a new class of hierarchical structures.[11-13]

Recently, a lot of research interests have been focused on incorporating multifunctional capabilities onto organic-inorganic nanohybrid systems with enhanced properties for various imaging and theranostic applications.[14-16] Multimodal imaging capabilities of nanosystems such as mesoporous silica,[17] gold nanoparticles (AuNPs),[18,19] polymers[20] and their hybrids have been studied extensively. In our previous research, hybrid materials consisting of mesoporous silica-graphene systems[21-23] and dye encapsulated micelles[24] were experimented, and their applications for various multimodal imaging were demonstrated. Assemblies of AuNPs may exhibit collective properties of localized surface plasmon resonance as a virtue of plasmonic coupling between the neighboring nanoparticles.[25-27] Small and finite interparticle gaps (in a nanometer range) generate several fold higher electromagnetic field on the metal surface than individual ones.[28,29] Thus, the controlled assembly and spatial arrangement of AuNPs have been

investigated along with a variety of systems, such as block copolymers, cationic polymers, semiconducting polymers, and silica, to tailor unique properties including photoacoustic imaging, photothermal effect, X-ray excited luminescence, surface enhanced Raman scattering, and so on.[30-34]

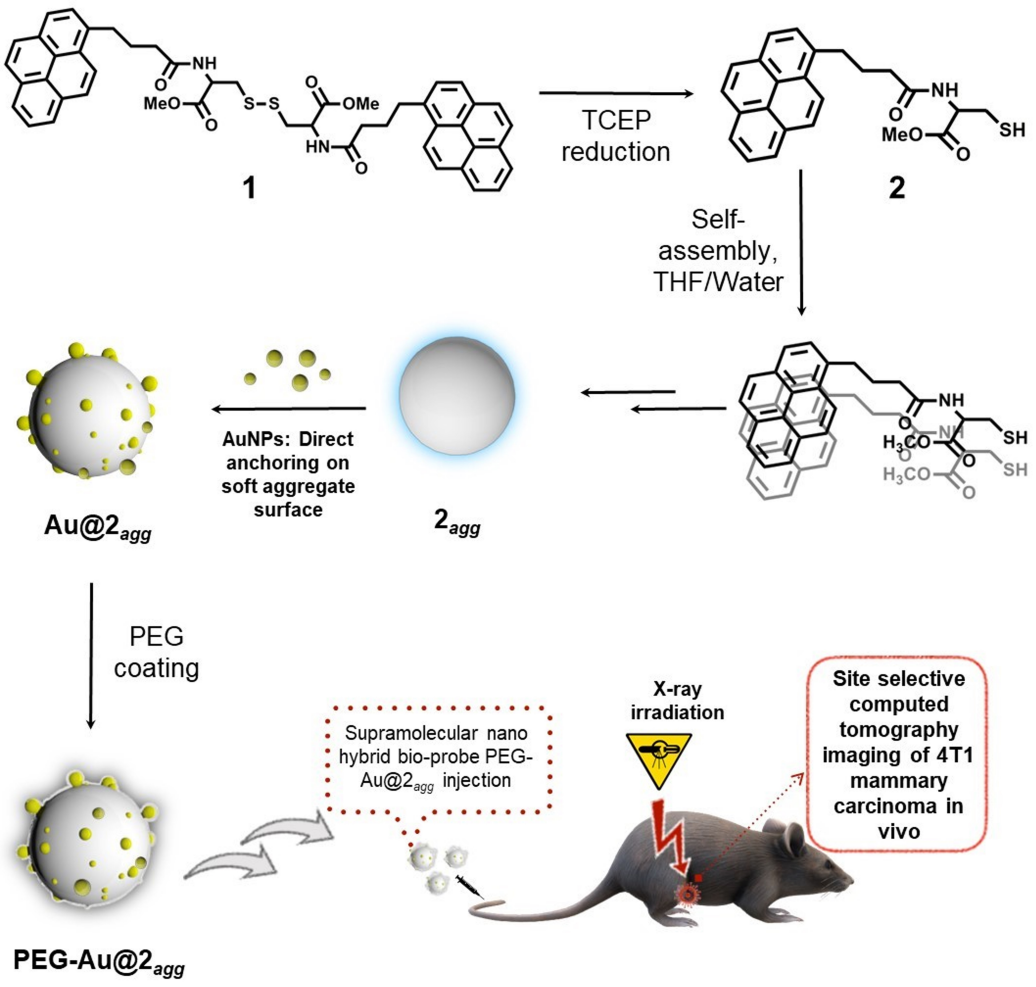

Scheme 1. Synthesis of compound 2, and illustration of self-assembly assisted formation of organic spherical aggregate (**2**$_{agg}$). Direct anchoring of AuNPs on **2**$_{agg}$ *via* Au-S interaction leading to **Au@2**$_{agg}$. PEG coating of **Au@2**$_{agg}$ affording final hybrid **PEG-Au@2**$_{agg}$.

In this work, we present a new design of organic-inorganic hybrid material through anchoring of plasmonic AuNPs on the surface of organic aggregates. For this purpose, a self-assembly of thiol tailed pyrene derivative (**2**) leads to the formation of nanosized organic spherical aggregate

(**2**$_{agg}$). Solvophobic self-assembly of **2** leaves thiol (-SH) rich surface of **2**$_{agg}$, allowing anchoring of external AuNPs through Au-S bond formation. Thus, AuNPs attaching on aggregate **2**$_{agg}$ to obtain hybrid **Au@2**$_{agg}$ followed by a biocompatible polyethylene glycol (PEG) coating were conducted to afford the final hybrid **PEG-Au@2**$_{agg}$ with interesting morphological features. The promising application potential of **PEG-Au@2**$_{agg}$ for *in vivo* site-selective tumor accumulation using micro X-ray computed tomography (CT) was then explored. Scheme 1 depicts the synthesis of **2** and the self-assembly process leading to final hybrid **PEG-Au@2**$_{agg}$ for X-ray CT application. The present work using supramolecular assembly strategy for the construction of organic-inorganic hybrid nanosystems demonstrates the excellent properties for tumor imaging *in vivo*.

Results and Discussion

Synthesis of thiol-tailed pyrene derivative **2** was achieved by using tris(2-carboxyethyl)phosphine (TCEP) mediated disulfide reduction of compound **1**.[35,36] A detailed procedure for the preparation of **1** *via* the reaction between 1-pyrenebutyric acid (polyaromatic core) and a cysteine residue with methyl protected α-carboxylic acid group is given in the Supporting Information. As-prepared **2** was purified using column chromatography and characterized by ^{1}H NMR, ^{13}C NMR and high-resolution mass spectrum techniques (Figure S1-S5). The specific self-assembly of compound **2** with exposed -SH functional group under solvophobic interactions leads to the formation of aggregate **2**$_{agg}$ having a net negative ζ (zeta)-potential (-27.6 ± 1.2 mV) on the surface (Figure S6). Next, the photophysical properties of **2** in various combinations of organic (tetrahydrofuran, THF) and aqueous solvent mixtures were studied. The changes in absorption and emission spectra of **2** in different THF/aqueous mixture solutions are shown in Figure S7 and S8, respectively. From solvent-dependent UV-Vis absorption spectroscopic analysis (Figure S7), broadening of characteristic peaks for **2** at 30:70

THF/water ratio was observed. Similarly, fluorescence emission spectra (Figure S8) exhibit prominent excimer emission at 479 nm upon increasing the content of water in THF solution of **2**, indicating the interaction of pyrene units in the assembly.

Nanometer sized spherical aggregates (**2**$_{agg}$) of compound **2** were then prepared. The experiments were performed in different solvent mixtures (THF/water, DMSO/water and DMF/water) and it was found that 30% THF / 70% water combination allows for the formation of suitable spherical aggregates (**Figure 1** and S9). Transmission electron microscopy (TEM) studies indicate the formation of nanometer sized spherical aggregates (**2**$_{agg}$) in 30% THF / 70% water solvent mixture (Figure 1a). In addition, the solution phase size distribution of **2**$_{agg}$ was monitored through dynamic light scattering (DLS) experiments (Figure 1h). The DLS measurement reveals a hydrodynamic diameter of 150 ± 20 nm with a narrow size distribution of **2**$_{agg}$. Hence, solvophobic effect and π-π stacking interaction mediate an induced aggregation on thiol-appended semi-amphiphilic pyrene derivative (**2**) in 30:70 THF/water mixture for the formation of spherical aggregates. To further investigate the proposed self-assembly mode of compound **2**, ^{1}H NMR titration studies in a mixture of THF-d_8 and D_2O were performed (Figure S10 and S11). Compound **2** is soluble in THF-d_8, whereas the addition of D_2O triggers its self-assembly for the formation of aggregates. As expected, upon increasing the D_2O percentage from 0 to 30%, a significant shift in the aromatic resonances (H_{11}-H_{17}) of the compound was observed (Figure S10). Interestingly, the resonance peak at 6.91 ppm corresponding to -N-H protons shows an upfield shift, clearly indicating prominent hydrogen bonding interaction at the cysteine thiol edge of compound **2** (Figure S11). This study indicates that, in 30:70 THF/water solution, the self-assembly of compound **2** obviously occurs to form the aggregates, mediated by π-π stacking and hydrogen bonding interactions. Fourier-transform infrared spectroscopic studies also corroborate the hydrogen bonding interactions with peak shifts in C=O and N-H regions (Figure S12). The characteristic peaks obtained from small-angle X-ray

scattering, wide-angle X-ray scattering, and low-angle powder X-ray diffraction of **2** and **2**$_{agg}$ indicate the π-π stacking interaction-assisted formation of supramolecular assembly (Figure S13-S15).

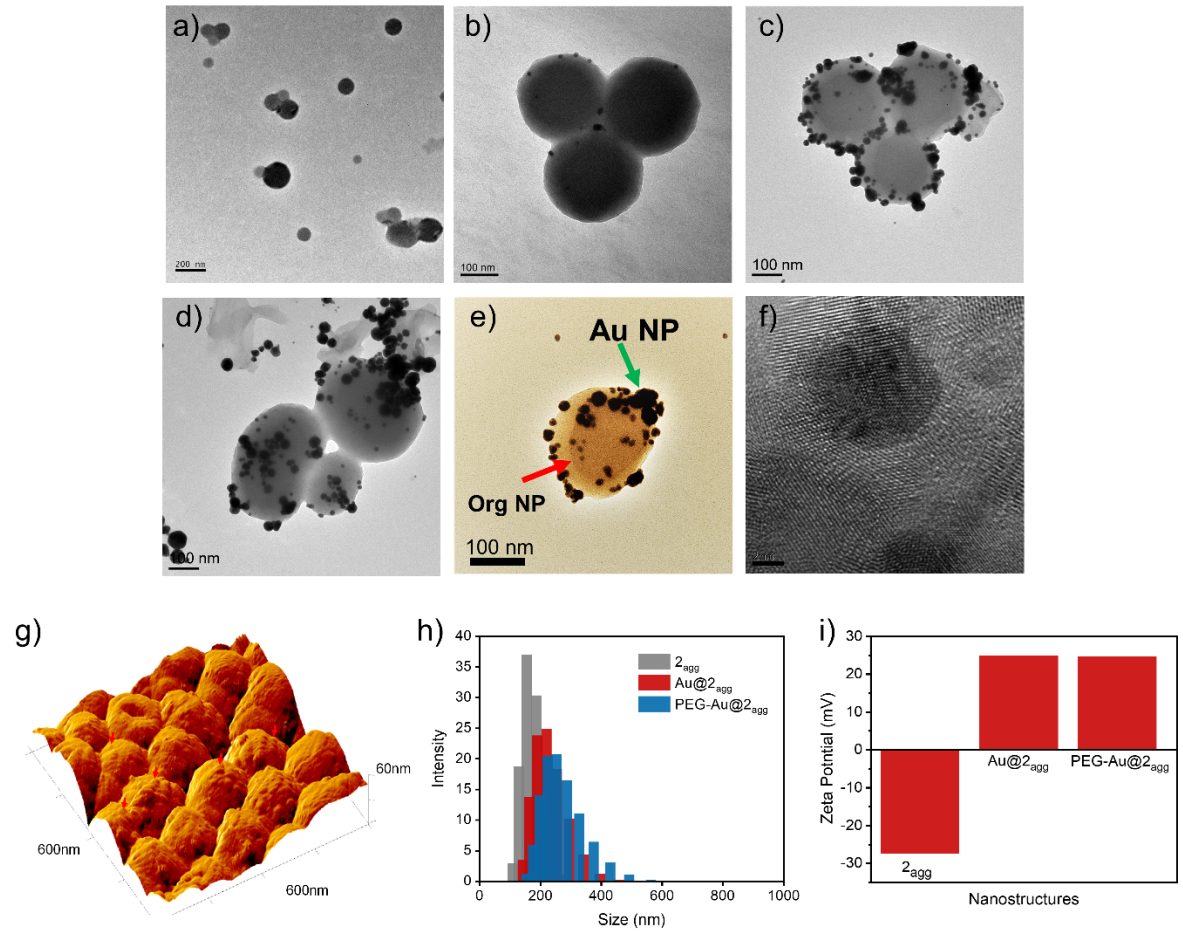

Figure 1. Morphological and surface properties of **2**$_{agg}$, **Au@2**$_{agg}$ and **PEG-Au@2**$_{agg}$. (a) TEM image of **2**$_{agg}$. TEM images showing the formation of **Au@2**$_{agg}$ under different stages at (b) 1 h, (c) 12 h, and (d) 24 h. (e) A pseudo-colored TEM image of **PEG-Au@2**$_{agg}$ after 24 h of formation. Red arrow indicates **2**$_{agg}$ and green arrow points toward anchored AuNPs. (f) High resolution TEM image of AuNPs anchored on the surface of **2**$_{agg}$. Scale bar: 2 nm. (g) AFM image (3D topography, 600 × 600 nm^2) of **PEG-Au@2**$_{agg}$ after 24 h, visualizing anchored AuNPs on the surface. Red arrows point toward anchored AuNPs. (h) DLS size and (i) ζ-potential variations of species at different stages of formation.

Next, direct anchoring of AuNPs (Figure S16) on the negatively charged surface of $\mathbf{2}_{agg}$ was performed by allowing the interaction of $\mathbf{2}_{agg}$ with polyethyleneimine (PEI) capped AuNPs for 24 h. In a typical reaction, $\mathbf{2}_{agg}$ (initial concentration = 5×10^{-5} M) was mixed with freshly prepared PEI coated AuNPs (0.5 mg mL^{-1}) in a 5 mL reaction vial with a constant stirring rate of 500 rpm for 24 h. The assembly was monitored with TEM at definite intervals for the formation of $\mathbf{Au@2}_{agg}$. TEM images of $\mathbf{Au@2}_{agg}$ at different time intervals are presented in Figure 1b-e. Direct anchoring of AuNPs on the surface of $\mathbf{2}_{agg}$ was evident, indicating the success of this anchoring approach. Interestingly, a reversal of surface potential was observed for $\mathbf{Au@2}_{agg}$ with a ζ-potential of 25 ± 0.5 mV, having an average size distribution of ~200 nm (Figure 1h,i). Therefore, strong electrostatic interaction[37,38] and thiol-Au bonding under a supramolecular assembly[39] lead to the formation of multicomponent hybrid $\mathbf{Au@2}_{agg}$. In order to enhance the biocompatibility of the hybrid, the coating of PEG-SH (molecular weight: 1000 Mn) was employed to afford the final hybrid $\mathbf{PEG\text{-}Au@2}_{agg}$.[40,41]

$\mathbf{PEG\text{-}Au@2}_{agg}$, a multicomponent organic-inorganic nanohybrid system, was formed *via* bottom-up self-assembly of components using integrated noncovalent and covalent interactions. High-resolution TEM images (Figure 1f and S17) show a single $\mathbf{PEG\text{-}Au@2}_{agg}$ nanoparticle having anchored AuNPs on an organic spherical substrate. Next, atomic force microscopy (AFM) imaging of $\mathbf{PEG\text{-}Au@2}_{agg}$ was performed using a Dimension Icon system (Bruker, USA) under tapping mode in fluid (deionized water). Three-dimensional (3D) topography of a colony of $\mathbf{PEG\text{-}Au@2}_{agg}$ with a height of *c.a.* 60 nm and an overall size of 120 nm on a mica surface is given in Figure 1g. Obviously evident contrast difference on the surface (Figure S18) indicates that anchored AuNPs are attached on the surface.

The effective anchoring of AuNPs on the surface of $\mathbf{2}_{agg}$ could also be monitored *via* changes in the UV/Vis absorption spectrum. **Figure 2a** shows the absorption spectral progress for the formation of $\mathbf{Au@2}_{agg}$ upon time-dependent deposition of AuNPs on $\mathbf{2}_{agg}$. Initially, a mixture

of **2**$_{agg}$ and AuNPs shows peaks at 337 nm and 353 nm corresponding to the pyrene unit, and a broad absorption around 500-600 nm assigned to plasmon absorption of AuNPs. Upon the deposition of AuNPs on **2**$_{agg}$, an interesting bathochromic shift (~11 nm) in the plasmon absorption of AuNPs at 530 nm was observed, indicating the formation of AuNP clusters in the hybrid. Figure 2b shows the absorption spectral comparison between AuNPs and final hybrid **PEG-Au@2**$_{agg}$. A photograph showing visible color change of these samples is also given (Figure S19).

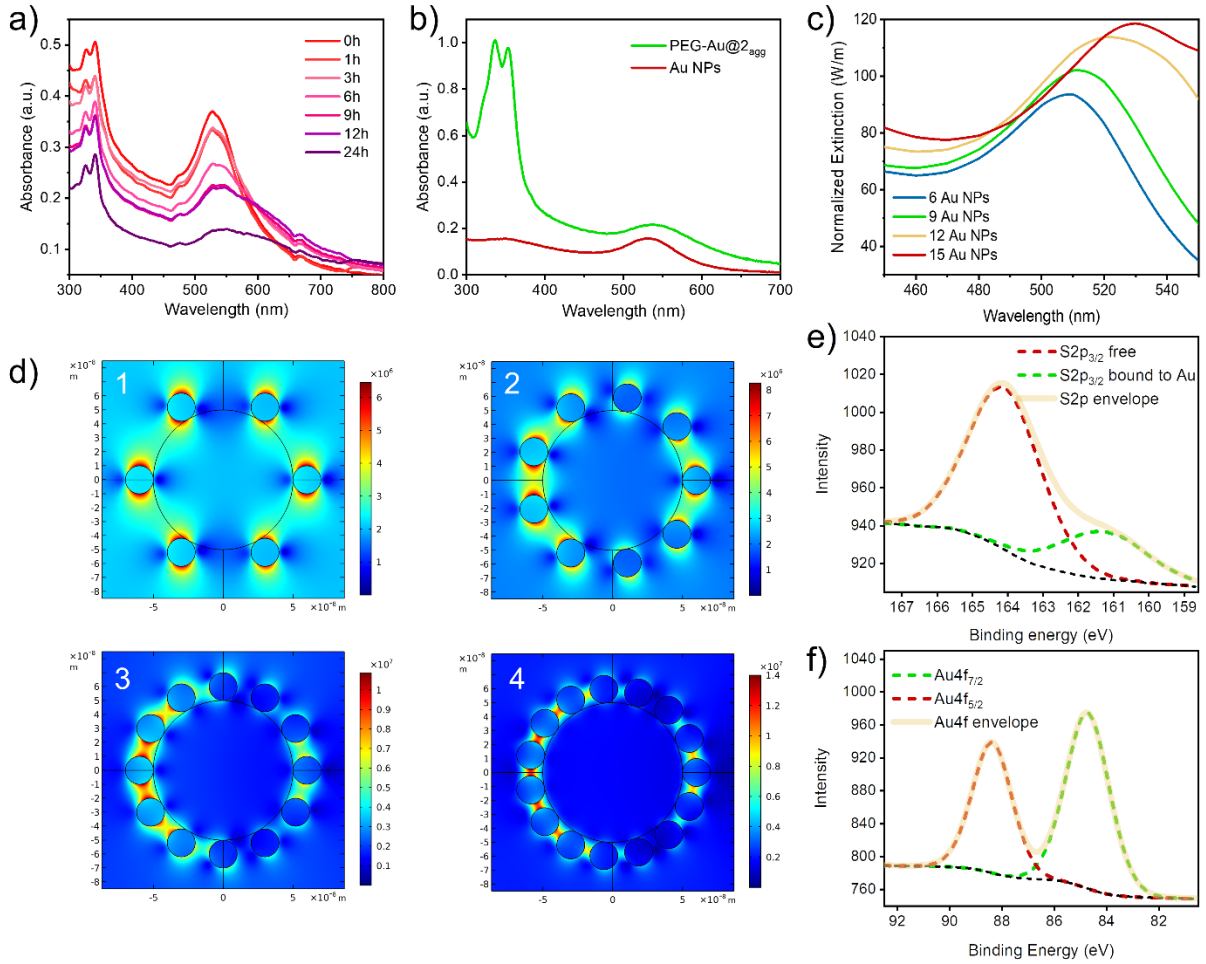

Figure 2. (a) Changes in UV-Vis absorption spectra monitored during the assembly of AuNPs on **2**$_{agg}$ for the formation of **Au@2**$_{agg}$ in PBS buffer at pH 7.4 until 24 h. (b) Absorption spectral comparison between AuNPs (red) and final hybrid **PEG-Au@2**$_{agg}$ (green) in PBS buffer at pH 7.4. (c) Simulated plasmon absorption changes of AuNPs on spherical aggregates depending on varied numbers (6, 9, 12, and 15) of AuNPs on the surface. (d) FEM simulation results

illustrating field intensity variation upon increasing the number of AuNPs on a spherical model. Figures 1–4 show field intensity variation with respect to the number (6, 9, 12, and 15) of AuNPs under a uniform size range. High resolution (e) XPS Sulfur spectra and (f) XPS gold spectra for **PEG-Au@2*agg*** showing changes in S2p and Au4f peaks.

We then investigated theoretically the physical process that governs the bathochromic plasmon shift in **Au@2*agg*** and conducted a numerical simulation using COMSOL Multiphysics under Finite Element Method (FEM). For this study, dielectric values of AuNPs were taken from intra-band model (Drude model) and fitted on Otter's data as per literature reports.[42,43] The simulations were conducted using electromagnetic wave frequency domain module with an input excitation of ~2 V/m of electric field intensity in *y*-direction and propagation in *x*-direction in aqueous medium. Our approach was to simulate the effect of (a) number of AuNPs on the surface on the plasmon absorption of the hybrid and (b) how the particle size of AuNPs affects the photophysical properties of the hybrid. Thus, a model **2*agg*** sphere of 100 nm diameter evenly covered with 20 nm AuNP spheres was employed, and the calculations were performed using equations as shown below (equations 1-3):[44]

$$P = \frac{1}{2} Re \left\{ \begin{vmatrix} H_z^* & -H_y^* & 0 \\ 0 & H_x^* & -H_z^* \\ -H_x^* & 0 & H_y^* \end{vmatrix} \begin{vmatrix} E_y \\ E_z \\ E_x \end{vmatrix} \right\} \qquad (1)$$

$$P_{sca} = \oint sum(P) \qquad (2)$$

$$P_{ext} = P_{abs} + P_{sca} \qquad (3)$$

where *H* and *E* stand for the far field scattered magnetic and electric field components solved by the program in respective axes denoted by their subscripts. The power absorbed (P_{abs} = $Q_r/t_{pulsewidth}$) by the AuNPs comprises mainly of resistive heating energy (Q_r) (equation 4) of the particles during the laser irradiation with the assumption of non-dissipative host medium.[45]

$$Q_r = \bar{J} \times \bar{E} \qquad (4)$$

where $\bar{J}$ and $\bar{E}$ represent the current density and electric field strength, respectively. A prominent plasmon absorption region from 450 to 600 nm was considered, where **2**$_{agg}$ remained optically transparent. Upon numerically varying the number of AuNPs on the surface of spherical assembly, the peak resonance of the collective system undergoes a red shift from 510 nm to 530 nm (Figure 2c). The field intensity variation at 525 nm corresponding to the assembly of 6-15 particles on the surface is shown in Figure 2d. Similarly, the size effect of AuNPs anchored on the surface of **2**$_{agg}$ was also evaluated. Figure S20a exhibits the changes in the absorption spectra of AuNPs upon varying the size from 10-20 nm. A 10 nm bathochromic shift in plasmon absorption of AuNPs was observed upon increasing the size, and a field intensity variation at 500 and 510 nm is given in Figure S20b. Hence, the observed shift in the plasmon absorption could be due to the collective effect of different sized AuNP clustering as well as the amount of AuNPs directly anchored on the surface of **2**$_{agg}$. Thus, the simulation results further provide solid evidence for the direct anchoring of AuNPs on **Au@2**$_{agg}$ during the time-dependent assembly process with corresponding changes induced in the plasmon absorption of AuNPs.

Notably, upon the formation of **Au@2**$_{agg}$ *via* anchoring of AuNPs on **2**$_{agg}$, the fluorescence emission from the aggregates undergoes significant quenching.[46] Figure S21 shows a comparison of emission spectra between **2**$_{agg}$ and **PEG-Au@2**$_{agg}$ and corresponding photographs of emission. Thus, **PEG-Au@2**$_{agg}$ shows no emission, which could be attributed to the well-known surface energy transfer process between the fluorophore mediated organic aggregates and AuNP clusters on the surface. Next, the presence of gold-thiol bond was determined by X-ray photoelectron spectroscopy (XPS) through comparing **2**$_{agg}$, AuNPs and **PEG-Au@2**$_{agg}$ (Figure 2e,f). The survey scans for **2**$_{agg}$ denote the presence of S, C, and O (Figure S22a), with AuNPs comprising Au, C, N, and O (Figure S22b) and **PEG-Au@2**$_{agg}$ indicating the presence of Au, S, C, N and O (Figure S22c). High resolution XPS for **2**$_{agg}$ reveals

that the sulfur photopeak $S_{2p3/2}$ at 164.19 eV corresponds to free thiol group on the surface of **2*agg*** (Figure S23a). Upon anchoring AuNPs on the surface, **PEG-Au@2*agg*** shows the presence of two doublets (Figure 2e) due to different chemical environments of the sulfur atoms. The one centered at 161.5 eV signals to the S-Au bond formation, while another peak at 164.19 eV corresponds to unbound sulfur on the surface. A doublet for Au $4f_{5/2}$ (87.7 eV) and $4f_{7/2}$ (84.0 eV) in the binding energy spectra (Figure S23b) indicates the characteristic Au(0) state from the control nanoparticle sample (AuNPs). The surface Au atoms of the nanoparticles binding to sulfur are potentially converted to Au(I).[39] In fact, a prominent peak shift of +0.7 eV for Au $4f_{7/2}$ (84.7 eV) confirms the presence of Au-S bond (Figure 2f).[47] The stability of the prepared hybrid **PEG-Au@2agg** was tested via Dynamic light scattering (DLS) study (Figure S24). The hybrid incubated in PBS pH 7.4 for 7 days exhibits negligible size variation over the course of 7 days, which confirms the size stability of hybrid in aqueous environments.

Detailed cytotoxicity assessment of **PEG-Au@2*agg*** was then conducted prior to investigating its bioimaging capability.[48] The cell viability of **PEG-Au@2*agg*** was evaluated using the MTT (3-(4,5-dimethylthiazolyl-2)-2,5-diphenyl-tetrazoliumbromide) viability assay on three different cell lines including HeLa, 4T1 and HepG2 cell lines (**Figure 3a**). The assay was carried out after incubating the hybrid at different concentrations for 24 h. All the cell lines maintain good cellular viability (>80%) for the given concentration range. Moreover, cell viabilities for **PEG-Au@2$_{agg}$** and non-PEGylated **Au@2$_{agg}$** were also compared by incubating them in 4T1 cell line (Figure S25). It was observed that a PEG encapsulation of **Au@2*agg*** reduces the toxicity of the hybrid significantly owing to the formation of dense brush on the surface of nanoparticles for suppressing phagocytic uptake *in vitro*.[49] The cells remain highly viable (>80%) for **PEG-Au@2$_{agg}$** with a concentration of 20 μM (3.5 ppm Au), whereas for **Au@2$_{agg}$**, the threshold of 80% is attained with 10 μM (1.75 ppm Au).

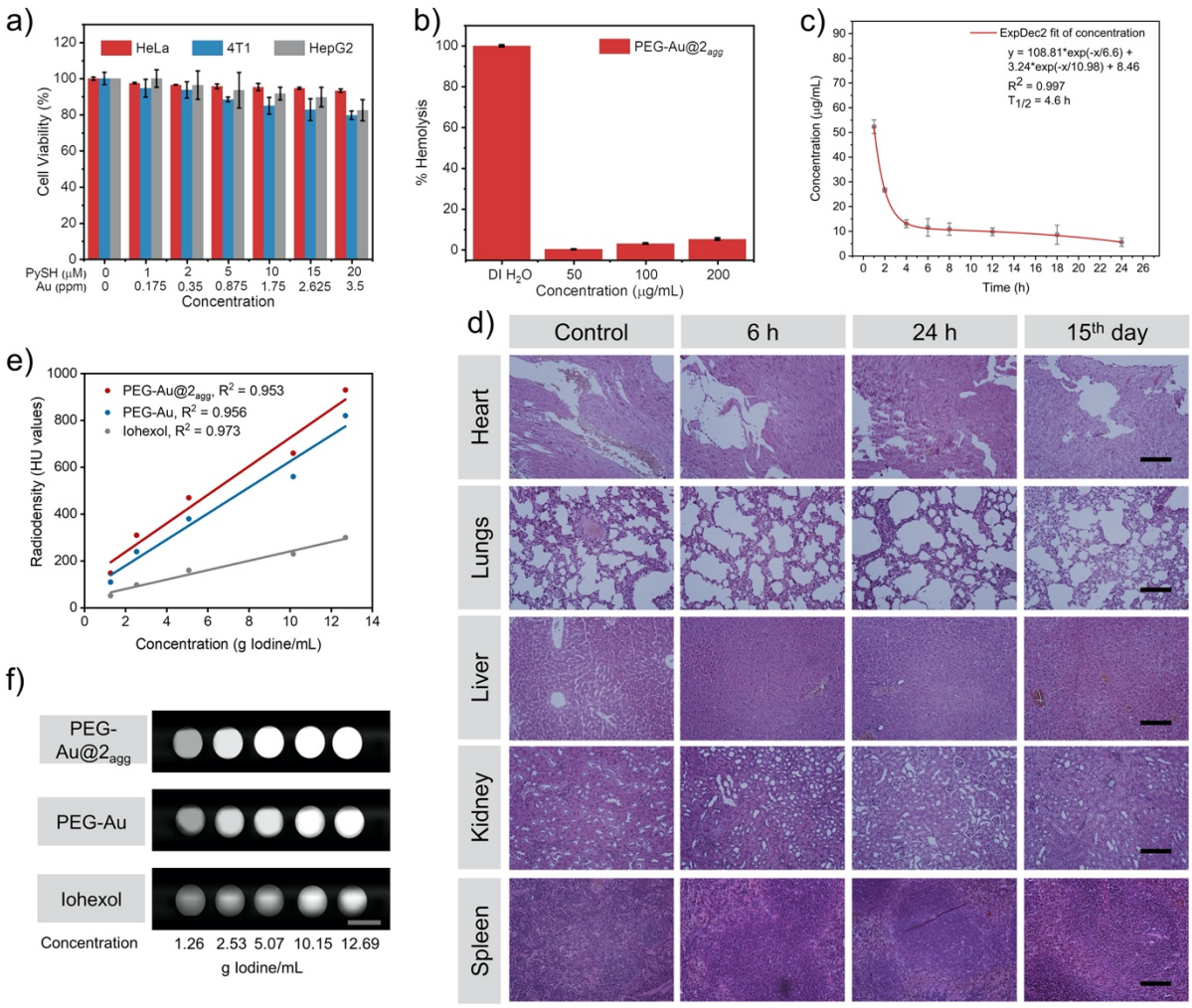

Figure 3. (a) *In vitro* cell viability of **PEG-Au@2*agg*** at different concentrations for 24 h in three different cell types: HeLa (red), 4T1 (blue) and HepG2 (grey). Data represent mean ± SE (n = 3). (b) Percentage hemolysis of **PEG-Au@2*agg*** at different concentrations. (c) Blood circulation lifetime of **PEG-Au@2*agg*** after intravenous injection into mice (n = 3). (d) Optical microscopy images showing the effect of **PEG-Au@2*agg*** on the histopathology of organs from Balb/c mice at various time intervals. Images were obtained with standard H&E stains. Scale bar is 100 μm. Comparison of CT imaging contrast as a function of concentration. (e) CT attenuation (HU) of **PEG-Au@2*agg*** in comparison with PEG-Au and iohexol at different concentrations (1.26 to 12.69 gI/mL). (f) CT images of **PEG-Au@2*agg***, PEG-Au and iohexol as a function of concentrations. Scale bar = 5 mm.

Concentration-dependent (50, 100 and 200 μg/mL) blood hemolysis analysis was conducted to evaluate the biosafety of **PEG-Au@2*agg*** (Figure 3b). During blood hemocompatibility check, deionized water and phosphate-buffered saline (PBS) at pH 7.4 were used as positive and negative controls, respectively. After 12 h post-incubation, the **PEG-Au@2*agg*** shows negligible hemolysis (c. a. 3%) at 100 μg/mL concentration while maximum hemolysis of c.a. 5% was calculated for a dose of highest concentration (200 μg/mL). Morphological features of blood cells after treating with **PEG-Au@2*agg*** remained intact as evident from scanning electron microscopy image measured 24 h after post-injection (Figure S26). To further understand the pharmacokinetics of **PEG-Au@2*agg*** in blood circulation after intravenous injection *via* tail vein, blood from mice was collected at 8 time points (1 h, 2 h, 4 h, 6 h, 8 h, 12 h, 18 h, and 24 h) to gauge the content of Au in the bloodstream using inductively coupled plasma – mass spectrometry (ICP-MS, Figure 3c). The blood distribution half-life ($t_{1/2\alpha}$) was calculated to be 4.6 ± 0.7 h, which is greater than half-life time of many AuNP systems reported.[50-52] The collected blood samples were also subjected to UV-Vis spectroscopy in the range of 500 – 600 nm to determine the amount of Au nanoparticles in the assembly of **PEG-Au@2*agg*** at various time points (Figure S27). These results suggest long blood circulation time coupled with regular and smooth distribution of **PEG-Au@2*agg*** *in vivo* owing to the PEG coating and the effective size of the nanoassembly for preventing premature removal by reticuloendothelial system.[53,54]

Prior to investigating the *in vivo* performance of **PEG-Au@2*agg***, biosafety and histological examinations were conducted. First of all, *in vivo* time-dependent toxicity evaluation of **PEG-Au@2*agg*** was performed in two animal groups (3 mice per group, see method section for more details): (i) PBS-injected mice (control) and (ii) **PEG-Au@2*agg*** -injected mice. Mice were observed at various time intervals to determine any injury or deleterious impact on the health of major organs including heart, lung, liver, spleen and kidney. Control (PBS-injected) and

PEG-Au@2$_{agg}$ treated mice showed similar body weights (Figure S28) with no hair loss or signs of injuries during planned course of observation.

To evaluate the *in vivo* systemic toxicity of **PEG-Au@2**$_{agg}$, animals from both groups were sacrificed at 6 h, 24 h and 15th day of planned study and major organs (heart, lungs, liver, spleen, and kidneys) were collected (Figure 3d). Hematoxylin and eosin (H&E) staining was used to understand possible pathological and histological changes of collected organs. The results of histological assessment confirm no pathological damage to the major organs when compared with the control group. The H&E analysis reveals that, myofiber and muscle bundle in heart are without any injury in the treated group, which are comparable to the controlled ones. Similarly, portal triad, hepatocyte and central vein in liver are also normal from the two groups at all studied times. In addition, glomerulus and tubules of kidney were observed without any type of histological change and tissue injury even after 15 days of treatment, again like the control group. Therefore, these results demonstrated that **PEG-Au@2**$_{agg}$ is safe to be used as a bioprobe for imaging modality *in vivo*.

At present, iodine containing small molecules have been used extensively for X-ray CT imaging. For these small molecules, limitations such as less number of contrast generating atoms present per molecule (typically 2-3) and their quick clearance through kidneys bring challenges for imaging.[55,56] Since gold with higher atomic number, at same concentration as that of iodine, is capable of producing 2.7 times higher contrast per unit weight than iodine, which in turn results in greater X-ray attenuation at lower dose (5.16 cm^2 g^{-1} at 100 keV). For the same reason, Au nanostructures have been extensively studied as contrast agents for X-ray CT imaging.[57-60] Regardless of the shape and size of AuNPs, the amount of Au per unit volume for X-ray CT imaging is an important criterion to induce strong X-ray attenuation.[61]

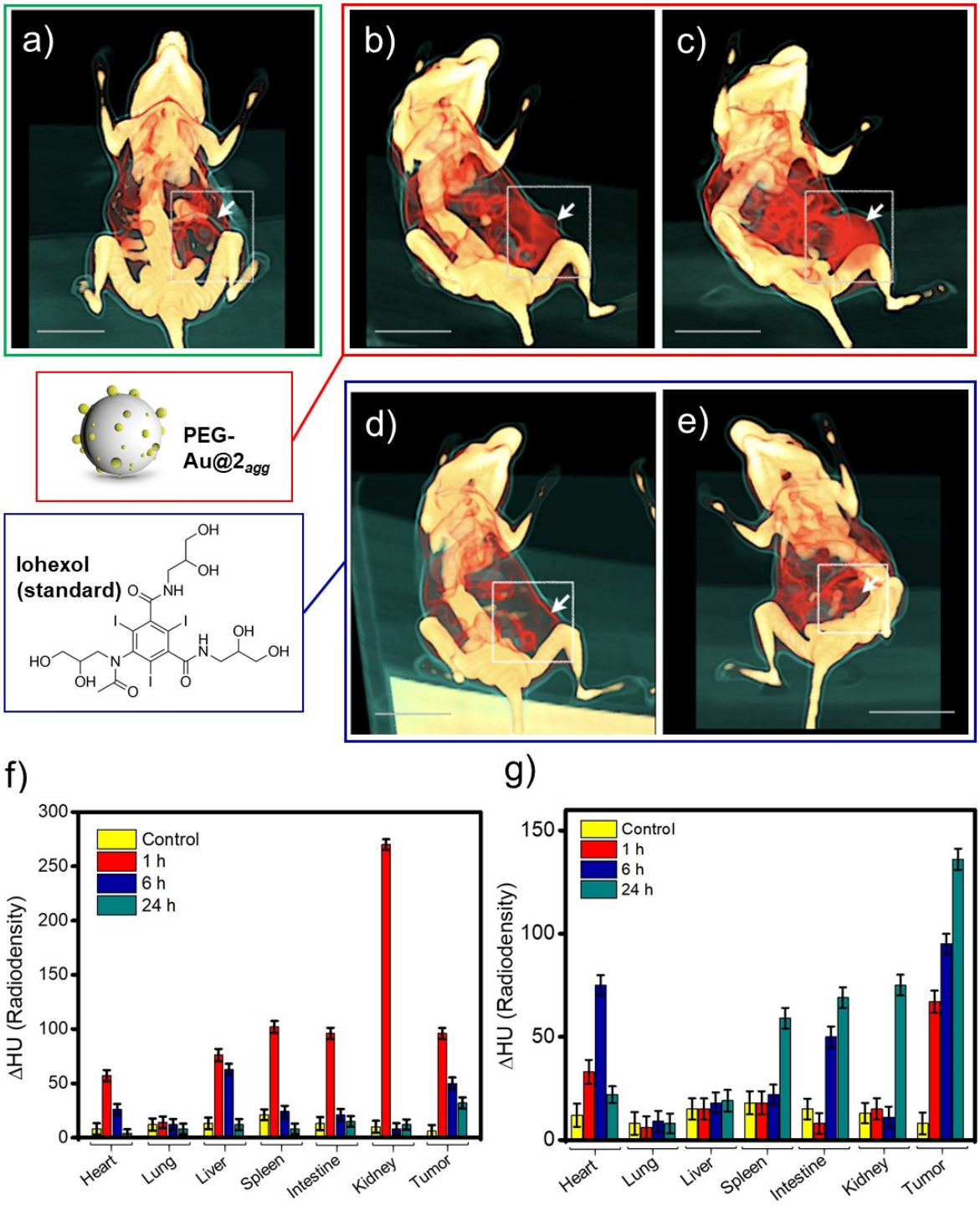

Figure 4. *In vivo* projection of X-ray CT images from 4T1 tumor bearing mice. (a) Whole body X-ray color-coded tomography image of a mouse before any treatment. Whole body X-ray color-coded tomography images of mice (b) 1 h and (c) 24 h post injection of **PEG-Au@2**$_{agg}$ and (d) 1 h and (e) 24 h post injection of iohexol. Radio intensity (ΔHU) data recorded in different organs with post injection of (f) iohexol and (g) **PEG-Au@2**$_{agg}$. Scale bar = 1 cm.

On account of unique features of **PEG-Au@2*agg*** and the presence of AuNPs on the surface of organic assembly, **PEG-Au@2*agg*** was expected to show an enhanced X-ray contrast when compared to the standard. To analyze X-ray attenuation capability of **PEG-Au@2*agg***, we compared it with a commonly used clinical contrast agent iohexol that contains iodine for CT imaging.[62] Figure 3e shows a CT image comparison between **PEG-Au@2*agg***, PEG-coated AuNPs (PEG-Au), and iohexol as the contrast agents at the same molar concentrations. A linear relationship between concentration and radiodensity (measured in Hounsfield units, HU) was observed upon increasing the concentrations of all samples. **PEG-Au@2*agg*** exhibits enhanced brightness and thus possesses significantly larger CT values than AuNPs and iohexol under same Au or I concentrations (Figure 3f). For example, at the concentration of 12.69 g I/mL (or 0.1 M), the X-ray attenuation of **PEG-Au@2$_{agg}$** is about 33 % higher than that of iohexol due to higher atomic number and electron density of Au as compared to I. In short, the *in vitro* CT imaging results corroborate that, on account of the anchoring of AuNPs on the surface of organic aggregates, the prepared **PEG-Au@2*agg*** possesses better X-ray CT imaging ability than individual AuNPs and clinically used iohexol.

The good biocompatibility of the **PEG-Au@2*agg*** hybrid along with its X-ray attenuation property *in vitro* encouraged us to pursue its CT contrast generation in animal models. To prove the contrast ability of **PEG-Au@2*agg*** *in vivo*, X-ray CT imaging was performed in six-week-old female BALB/c mice expressing 4T1 tumor. After injecting the **PEG-Au@2*agg*** hybrid intratumorally, CT scans were captured at various time intervals, *i.e.*, 1 h, 6 h, and 24 h post-injection. Simultaneously, iohexol was also injected and analyzed using another set of animals. **Figure 4** shows X-ray micro radiology image results obtained by pre/post-injection of **PEG-Au@2*agg*** and iohexol recorded at different time intervals (1 h and 24 h post injection). Figure 4a depicts the projection views of CT scans from the mice without the injection of **PEG-**

Au@2$_{agg}$ or iohexol (namely 'pre-injected mice'), and no detectable contrast was observed. After intratumoral injection of **PEG-Au@2**$_{agg}$ (10 mg kg^{-1} body weight, 200 µL), tomographically reconstructed projection of X-ray images from 4T1 tumor bearing mice are shown in Figure 4b,c. Intense red color (labelled in dotted square) indicates tumor sites. These data were acquired after 1 h and 24 h respectively, presenting significant intensity enhancement and accumulation of **PEG-Au@2**$_{agg}$ in the tumor sites. Overall, a maximum radiodensity value was recorded after 24 h post-injection of **PEG-Au@2**$_{agg}$, whereas other organs show relatively lower accumulation.[63] Interestingly, mice injected with iohexol (Figure 4d,e) exhibit minimal tumor accumulation after 24 h owing to the rapid clearance from the body.

During X-ray radiography experiments, the radiodensity in all major organs as well as 4T1 tumor sites was recorded at different time intervals for both iohexol and **PEG-Au@2**$_{agg}$ groups as illustrated in Figure 4f,g. *In vivo* X-ray intensity of internal organs with post-injection of iohexol (Figure 4f) exhibits the maxima at 1 h, and subsequently iohexol gets washed out via the renal clearance to give a reduced contrast in the tumor region, as evident from lower HU value (ΔHU = 33.4) at the tumor sites, indicating nonspecific biodistribution and rapid clearance of the small molecule iohexol from the body. More importantly, **PEG-Au@2**$_{agg}$ exhibits an enhanced contrast at post-injection (Figure 4g) with the maximum in the tumor sites attained at 24 h (ΔHU = 141). The observed 4.2-fold enhanced accumulation of **PEG-Au@2**$_{agg}$ on 4T1 tumor sites could be attributed to larger vascular endothelium in 4T1 tumor model, leading to vasculature-based differential tumor uptake. Axial *in vivo* and *ex vivo* CT images for major organs were also acquired after 1 h and 24 h post injection (Figure S29). Strong contrast in the bladder region was noticed in 1 h of post-injection with iohexol, whereas the bladder region of mice receiving **PEG-Au@2**$_{agg}$ showed negligible contrast and stayed non-detectable until 24 h, thereby suggesting the clearance of iohexol within an hour of injection.

Tumor targeting and homing capability of the prepared nanohybrid **PEG-Au@2*agg*** upon intravenous injection for systemic circulation were explored and compared with iohexol and PEG-Au (Figure S30 and Table S1-S3). The contrast of PEG-Au in tumor sites (ΔHU 98 after 1 h, ΔHU 142 after 6 h and ΔHU 177 after 24 h of post-injection) was significantly lower when compared to the prepared **PEG-Au@2*agg*** (ΔHU 120 after 1 h, ΔHU 189 after 6 h and ΔHU 224 after 24 h of post-injection). The accumulation of **PEG-Au@2*agg*** in tumor upon systemic administration was found to be ~16.26% injected dose per gram (%ID/g, Figure S31). **PEG-Au@2*agg*** thereby shows higher and stronger tumor binding ability than PEG-Au and iohexol, thus indicating the impact of surface anchoring approach of AuNPs onto the soft assembly of **2*agg***. In addition to the considerations related to nanoparticle interaction with hepatic and renal systems, it is important to study the efficacy of the prepared nanohybrid on different tumor volumes, as the cancer pathophysiology can influence tumor targeting, accumulation, and penetration.[64] To address these concerns, *ex-vivo* X-ray computed tomography scans of tumors with different sizes (~93.6 mm^3, ~114.4 mm^3, and ~130.9 mm^3) were investigated 24 h post intravenous injection of **PEG-Au@2*agg*** (Figure S32). It was found that, regardless of the tumor size, **PEG-Au@2*agg*** exhibits remarkable radiocontrast intensity signals with clear visualization of tumor, demonstrating superiority of the hybrid as an X-ray CT contrast agent for varying tumor volumes.

Conclusion

Successful development of an organic-inorganic nanohybrid by direct anchoring of AuNPs on self-assembled organic nanostructure has been demonstrated. Bottom-up formation approach of self-assembled spherical aggregate (**2*agg***) from thiol-tailed pyrene derivative (**2**) and direct anchoring of AuNPs on the surface by making use of Au-S interaction followed by PEGylation has been established to achieve the **PEG-Au@2*agg*** nanohybrid. Structurally engineered **PEG-**

Au@2$_{agg}$ is a promising contrast agent and bioprobe for *in vivo* site-selective tumor accumulation, demonstrating X-ray micro-CT imaging in 4T1 tumor bearing mice model. Thus, we have demonstrated a self-assembly based strategy to enhance X-ray CT contrast by locally anchoring the attenuation agent AuNPs on the surface of a supramolecular assembly. The approach presented in this work would provide a new direction in the development of next generation contrast agents and bioprobes for disease diagnosis and imaging.

Experimental Section

Synthesis of 1: As shown in Scheme S1, 4-pyrenebutyric acid (500 mg, 1.24 mmol) was dissolved in anhydrous DMF (5 mL), and *N*-[(dimethylamino)-1H-1,2,3-triazolo-[4,5-b]pyridin-1-ylmethylene]-*N*-methylmethanaminium hexafluorophosphate *N*-oxide (563.96 mg, 1.48 mmol) was added to the stirring solution, followed by the addition of *N*,*N*-diisopropylethylamine (473.62 μL, 2.72 mmol). After 20 min of stirring, methyl protected cysteine residue (165.84 mg, 0.62 mmol) was added, and the reaction was left to stir at room temperature under nitrogen atmosphere for 24 h. A saturated solution of sodium chloride was added to the round bottom flask and the mixture was cooled to 4 ºC to yield a white precipitate. The white precipitate was washed with deionized water and collected by vacuum filtration. The crude product was purified by silica gel column chromatography with 70% dichloromethane : 30% ethyl acetate. ^{1}H NMR (300 MHz, $CDCl_3$, δ) 8.24 (d, J = 9.3 Hz, 1H), 8.13 (d, J = 7.6 Hz, 2H), 8.07 (d, J = 2.8 Hz, 1H), 8.04 (s, 1H), 7.98 (s, 2H), 7.95 (d, J = 8.1 Hz, 1H), 7.80 (d, J = 7.8 Hz, 1H), 6.37 (d, J = 7.3 Hz, 1H), 4.90 – 4.81 (m, 1H), 3.71 (s, 3H), 3.32 (t, J = 7.5 Hz, 2H), 3.15 (d, J = 5.2 Hz, 2H), 2.37 – 2.27 (m, 2H), 2.17 (q, J = 6.9 Hz, 2H), 1.26 (s, 1H), 0.88 (s, 0H). Mass calculated for $C_{48}H_{44}N_2O_6S_2$ m/z: 807.03, found m/z: 809.2716 [M+H]. ^{1}H NMR and HR-MS spectra are shown in Figures S1 and S2, respectively.

Synthesis of 2: To a stirring solution of compound **1** (63.80 mg, 0.08 mmol) in THF (10 mL), tris(2-carboxyethyl)phosphine hydrochloride (226.33 mg) in deionized water (1 mL) was added, and the mixture was allowed to stir at room temperature for 18 h. The successful cleavage of disulfide to thiol was monitored by thin layer chromatography, and the volatiles were removed by rotary evaporation. Then, the reaction mixture was extracted with $CHCl_3$ to give the thiol containing compound **2**. ^{1}H NMR (300 MHz, $CDCl_3$, δ) 8.36 (d, J = 87.3 Hz, 1H), 8.18 – 8.08 (m, 2H), 8.05 – 7.99 (m, 1H), 7.94 (s, 1H), 3.86 (s, 2H), 3.48 (s, 2H), 3.48 (s, 1H), 3.10 (s, 1H), 2.48 (s, 2H), 2.29 (s, 1H), 1.56 (s, 13H), 1.30 (dd, J = 17.2, 8.2 Hz, 1H). ^{13}C NMR (500 MHz, $CDCl_3$) δ 172.55, 170.77, 135.78, 131.56, 131.05, 130.14, 128.92, 127.57 (d, J = 6.2 Hz), 126.88, 125.99, 125.25, 125.15 – 124.83 (m), 123.46, 53.58, 52.94, 35.91, 32.82, 27.31, 27.04. Mass calculated for $C_{24}H_{23}NO_3S$ m/z: 405.14, found m/z: 406.21 [M+H]. ^{1}H NMR, ^{13}C NMR and HR-MS spectra are shown in Figures S3-S5.

Self-Assembly of 2 in THF/Water Mixture to Form $\mathbf{2}_{agg}$: The $\mathbf{2}_{agg}$ organic aggregate was prepared by the reprecipitation method (see Supporting Information for detailed trials in different solvent mixtures). In a typical procedure, **2** solution (100 μL, 0.5 mM) in THF was injected dropwise into distilled water (700 μL) under sonication for over 30 min and stirred (800 rpm) at room temperature overnight to evaporate THF slowly. The obtained $\mathbf{2}_{agg}$ organic aggregate solution was centrifuged at 10000 rpm and stored at 4 ºC for further use. The shape and size of the resulting $\mathbf{2}_{agg}$ organic aggregate were determined by TEM and DLS. Zeta potential measurements were carried out to confirm the size distribution and surface charge.

Synthesis and characterizations of PEI-Capped AuNPs: AuNPs with PEI capping were prepared according to the method by Song *et al.*[65] with some modifications. An aqueous solution of $HAuCl_4$ (14 mM, 25 mL) was added with 1% w/w PEI (50 kDa), which was stirred vigorously at room temperature for 24 h and thereafter heated at 70 ºC for 1 h. As synthesized PEI stabilized AuNPs were concentrated and centrifuged using 100K cut-off ultracentrifuge

membrane tube filter to remove excess PEI. Figure S16 shows TEM image, UV-Vis absorption spectrum, and DLS measurements (size distributions and ζ-potential values) of freshly prepared AuNPs.

Direct Anchoring of AuNPs onto Self-Assembled $\mathbf{2}_{agg}$ Nanoparticles: The prepared AuNP solution (50 μL, 4.34 mM) was added to the $\mathbf{2}_{agg}$ solution (1 mL, 5×10^{-5} M) under stirring. The solution was stirred for 24 h and **Au@2**$_{agg}$ was separated *via* centrifugation at 8000 rpm for 30 mins. The solution was then washed twice with distilled water to remove any unattached AuNPs. **Au@2**$_{agg}$ was stored in dark at 4 °C until further use.

PEG-SH coating of Au@2$_{agg}$: Au@2$_{agg}$ was stirred with PEG-SH_{2k} in 1:5 mass ratio in distilled water at room temperature for 12 h. The resulting **PEG-Au@2**$_{agg}$ hybrid was centrifuged and washed twice to remove unattached PEG-SH, and stored in dark at 4 °C until further use.

MTT Assay for Cytotoxicity Studies: For cytotoxicity measurements, the cells (HeLa, HepG2, and 4T1) were trypsinized, and 1×10^4 cells were seeded per well in the 96-well plate. After incubating the cells overnight, the exhausted medium was replaced with a fresh medium (100 μL) containing various concentrations of the **PEG-Au@2**$_{agg}$ assembly. Following the incubation for another 24 h with the assembly, the medium was replaced with a fresh medium containing 10% MTT (0.5 mg mL^{-1}). After incubating the cells for 4 h, the medium was removed and DMSO (100μL) was added. The absorbance at 570 nm wavelength was measured using 96-well microplate reader. Cell viability was calculated by keeping PBS dissolved in the medium as the control according to $[A]_{sample}/[A]_{control} \times 100\%$, where $[A]_{sample}$ denotes average absorption intensity of the sample containing the assembly, and $[A]_{control}$ is the average absorption intensity of the control PBS.

***In Vivo* Toxicity Study**. *In vivo* toxicity of **PEG-Au@2**$_{agg}$ was validated by performing blood biochemistry hemolysis analysis, histopathological examinations (H&E), body weight and

health measurements. Various concentrations (50, 100 and 200 μg mL^{-1}) of fabricated **PEG-Au@2*agg*** were used for blood biochemistry/hemolysis experiments. We adopted the experimental protocol from previously reported method with some modifications.[66] 40 μL of blood from healthy mice was collected in ethylenediaminetetraacetic acid stabilized tubes. Collected red blood cells were then diluted with PBS. RBCs (500 μL) were treated with various concentrations (50-200 μg mL^{-1}) of nanohybrids for a period of 12 h at room temperature and then centrifuged at 4000 rpm for 10 min. Deionized water and PBS were used as positive and negative controls in the hemolysis procedure. Percentage hemolysis values were calculated using the equation: % hemolysis = [(absorbance of the used sample - absorbance of negative control) / (positive control absorbance - negative control absorbance)] × 100.

Next, a single dose of **PEG-Au@2*agg*** dispersed in PBS (10 mg kg^{-1} body weight; 200μL) was intravenously injected into female Balb/c mice to evaluate the body weight and health measurements, blood circulation/pharmacokinetic behavior of injected nanohybrids and histopathological examinations of major organs. Moreover, the presence of gold in blood was confirmed by ICP-MS and spectroscopic analysis to study the blood circulation of injected nanohybrid. In brief, 40 μL blood was collected from tail vein at various time points of post administration (1 h, 2 h, 4 h, 6 h, 8 h, 12 h, 18 h, and 24 h) of **PEG-Au@2*agg*** and used for ICP-MS and spectroscopic analysis. Furthermore, these blood samples (AuNP-contained blood) were processed in aqua regia for ICP-MS measurements. For the spectroscopic measurements, the blood samples were centrifuged at 1000 g for 10 min, and the obtained AuNP pellets were studied for absorbance spectroscopy. Animal body weight measurement, hair loss, and normal behavior were observed every day for over 15 days course. At various time point (6 h, 24 h, and 15^{th} day), mice were sacrificed (n = 3/group) for H&E staining of tissues from heart, lung, liver, spleen, and kidney to investigate the tissue injury.

CT Imaging (Radiodensity Measurement). PEG-Au@2*agg* assembly, PEG-Au, and iohexol (equivalent 1.26 – 12.69 g I mL^{-1} concentrations) were investigated to evaluate the contrast ability *in vitro*. Aqueous solutions of each system with different concentrations were prepared in plastic eppendorf tubes and placed in scanning holder. The X-ray attenuation was calculated by using following equations (5-7).

$$I = Io e^{-\mu x} \quad (5)$$

$$\mu = \frac{PZ^4}{AE^3} \quad (6)$$

$$\mu = \frac{(\mu sample - \mu water)}{\mu water} \times 1000 \quad (7)$$

where I = transmitted X-ray, I_0 = incident X-ray, E = X-ray energy, Z = atomic number, P = density, A = atomic mass, and X = thickness of matrix/sample.

To examine the *in vivo* biodistribution and localized tumor diagnosis, 10 mg kg^{-1} body weight dose of **PEG-Au@2*agg*** was injected intratumorally in 4T1 tumor bearing mice (~16 g body weight). CT scans at 100 kV and 50 mA on **PEG-Au@2*agg*** injected mice were captured at various time points (1 to 24 h). The radiodensity comparison of major organs and tumor sites after injecting **PEG-Au@2*agg*** and iodinated contrast agents were also made. All scans were performed with 64 simultaneous 0.5 mm slices per rotation using clinical CT scanner (GE Medical Systems, HiSpeed NX/i) at 100 kV tube voltage and 50 mA tube current, HELICAL Mode, 64 simultaneous 3.0 mm slice thickness, 0.35 spatial resolution, 350.0 reconstruction Diameter, Instance number 8 with Pixel Spacing 0.683594, reconstruction algorithm value 13, increment/focal spot 1.2, pitch 949.075. For tumor targeting and tumor size-dependent contrast studies, **PEG-Au@2*agg*** (10 mg kg^{-1} body weight) was injected intravenously *via* tail vein in 4T1 tumor bearing mice (~20 g body weight). The radiodensity was measured in HU for each by using RadiAnt DICOM Viewer software and following equation:

Radiodensity (HU) = (HU value of suspended system - HU value of water) / (HU value of water - HU value of air) (8)

Animal Models and Tumor Growth. All experimental protocols involving mice were approved by the Institutional Animal Care and Use Committee (IACUC) of National Centre for Cell Science, and the Institutional Animal Care and Use Committee of Nanyang Technological University (NTU-IACUC) with a protocol number of A18012. In total, six-week-old female BALB/c mice were injected with 4T1 cells (1×10^5) into mammary fat pad, and tumor cells were then left to grow for one week. After tumors reached to approximately 100 mm^3 in size, mice were administered intratumorally with **PEG-Au@2**$_{agg}$ (10 mg kg^{-1} body weight).

Statistical analysis: The representative data measured were expressed as mean ± SD. Statistical analysis was performed using a student's t test. Statistically significant difference was represented as *$p < 0.05$, **$p < 0.01$, and ***$p < 0.001$.

Supporting Information

Supporting Information is available from the Wiley Online Library or from the author.

Acknowledgements

A.K.B. and Y.L.Z thank the Singapore Agency for Science, Technology and Research (A*STAR) AME IRG grant (No. A20E5c0081), and the Singapore National Research Foundation Investigatorship (No. NRF-NRFI2018-03). S.S. and C.T.L. thank iHealthtech-NUS for financial support. R.P. acknowledges IIT-Bombay for awarding Institute Post-Doctoral Fellowship. R.S. thanks the Department of Biotechnology National Bioscience Award, Govt. of India. We thank Mr. Pinaki, NCCS, Pune for Animal House Facility and providing animals for the study, Dr. Narendra Gupta (MD, Radiologist) and Dr. Mirapgar (MD, Radiologist) for discussing X-ray CT images.

References

[1] E. Mattia, S. Otto, *Nat. Nanotechnol*. **2015**, *10*, 111-119.

[2] A. J. Savyasachi, O. Kotova, S. Shanmugaraju, S. J. Bradberry, G. M. Ó'Máille, T. Gunnlaugsson, *Chem* **2017**, *3*, 764-811.

[3] X. Ma, Y. Zhao, *Chem. Rev.* **2015**, *115*, 7794-7794.

[4] S.S. Babu, V.K. Praveen, A. Ajayaghosh, *Chem. Rev.* **2014**, *114*, 1973-2129.

[5] P. Xing, Y. Zhao, *Adv. Mater.* **2016**, *28*, 7304-7339.

[6] Z. Nie, A. Petukhova, E. Kumacheva, *Nat. Nanotechnol.* **2010**, *5*, 15-25.

[7] W. Li, I. Kanyo, C. H. Kuo, S. Thanneeru, J. He, *Nanoscale* **2015**, *7*, 956-964.

[8] N. Gong, X. Ma, X. Ye, Q. Zhou, X. Chen, X. Tan, S. Yao, S. Huo, T. Zhang, S. Chen, X. Teng, X. Hu, J. Yu, Y. Gan, H. Jiang, J. Li, X.J. Liang, *Nat. Nanotechnol.* **2019**, *14*, 379-387.

[9] F. Ishiwari, Y. Shoji, T. Fukushima, *Chem. Sci.* **2018**, *9*, 2028-2041.

[10] Q. Zhang, Y.-X. Deng, H.-X. Luo, C.-Y. Shi, G. M. Geise, B. L. Feringa, H. Tian, D.-H. Qu, *J. Am. Chem. Soc.* **2019**, *141*, 12804-12814.

[11] S. K. Maji, A. K. Mandal, K. T. Nguyen, P. Borah, Y. Zhao, *ACS Appl. Mater. Interfaces* **2015**, *7*, 9807-9816.

[12] S. K. Maji, A. K. Mandal, K. T. Nguyen, P. Borah, Y. Zhao, *ACS Appl. Mater. Interfaces* **2014**, *6*, 13648-13656.

[13] P. Wang, S. Gaitanaros, S. Lee, M. Bathe, W. M. Shih, Y. Ke, W. H. Coulter, *J. Am. Chem. Soc.* **2016**, *138*, 7733-7740.

[14] N. Zhao, L. Yan, X. Zhao, X. Chen, A. Li, D. Zheng, X. Zhou, X. Dai, F. J. Xu, *Chem. Rev.* **2019**, *119*, 1666-1762.

[15] I. Pastoriza-Santos, C. Kinnear, J. Pérez-Juste, P. Mulvaney, L. M. Liz-Marzán, *Nat. Rev. Mater.* **2018**, *3*, 375-391.

[16] G. Yang, S. Z. F. Phua, W. Q. Lim, R. Zhang, L. Feng, G. Liu, H. Wu, A. K. Bindra, D. Jana, Z. Liu, Y. L. Zhao, *Adv. Mater.* **2019**, *31*, 1901513.

[17] L. Z. Zhao, W. Yuan, C. Y. Ang, Q, Y. Qu, Y. Dai, Y. L. Gao, Z. Luo, J. G. Wang, H. Z. Chen, M. H. Li, F. Li. Y. L. Zhao, *Adv. Funct. Mater.* **2016**, *26*, 3036-3047.

[18] R. Zhu, H. Feng, Q. Li, L. Su, Q. Fu, J. Li, J. Song, H. Yang, *Angew. Chem. Int. Ed.* **2021**, *60*, 12560-12568.

[19] X. Zhang, Z.-W. Li, Y. Wu, X. Ge, L. Su, H. Feng, Z. Wu, H. Yang, J. Song, *Angew. Chem. Int. Ed.* **2021**, *60*, 17647-17653.

[20] M. Nakayama, W. Q. Lim, S. Kajiyama, A. Kumamoto,Y. Ikuhara, T. Kato, Y. Zhao, *ACS Appl. Mater. Interfaces* **2019**, *11*, 17759-17765.

[21] S. Sreejith, X. Ma, Y. Zhao, *J. Am. Chem. Soc.* **2012**, *134*, 17346-17349.

[22] K. T. Nguyen, Y. Zhao, *Acc. Chem. Res.* **2015**, *48*, 3016-3025.

[23] K. T. Nguyen, S. Sreejith, J. Joseph, T. He, P. Borah, E. Y. Guan, S. W. Lye, H. Sun, Y. Zhao, *Part. Part. Syst. Charact.* **2014**, *31*, 1060-1066.

[24] S. Sreejith, J. Joseph, M. Lin, N. V. Menon, P. Borah, H. J. Ng, Y. X. Loong, Y. Kang, S. W. K. Yu, Y. Zhao, *ACS Nano* **2015**, *9*, 5695-5704.

[25] H. Sun, J. Du, *Nanoscale* **2018**, *10*, 17354-17361.

[26] R. M. Gorgoll, T. Tsubota, K. Harano, E. Nakamura, *J. Am. Chem. Soc.* **2015**, *137*, 7568-7571.

[27] K. Saha, S. S. Agasti, C. Kim, X. Li, V. M. Rotello, *Chem. Rev.* **2012**, *112*, 2739-2779.

[28] C. Wang, D. Astruc, *Chem. Soc. Rev.* **2014**, *43*, 7188-7216.

[29] A. Klinkova, R. M. Choueiri, E. Kumacheva, *Chem. Soc. Rev.* **2014**, *43*, 3976-3991.

[30] Y. Liu, J. He, K. Yang, C. Yi, Y. Liu, L. Nie, N. M. Khashab, X. Chen, Z. Nie, *Angew. Chem. Int. Ed.* **2015**, *54*, 15809-15812.

[31] W. Sun, L. Luo, Y. Feng, Y. Cai, Y. Zhuang, R. J. Xie, X. Chen, H. Chen, *Angew. Chem. Int. Ed.* **2020**, *59*, 9914-9921.

[32] Z. Yang, J. Song, Y. Dai, J. Chen, F. Wang, L. Lin, Y. Liu, F. Zhang, G. Yu, Z. Zhou, W. Fan, W. Huang, Q. Fan, X. Chen, *Theranostics* **2017**, *7*, 2177-2185.

[33] Z. Wang, D. Shao, Z. Chang, M. Lu, Y. Wang, J. Yue, D. Yang, M. Li, Q. Xu, W. Dong, *ACS Nano* **2017**, *11*, 12732-12741.

[34] N. Castro, D. Constantin, P. Davidson, B. Abécassis, *Soft Matter* **2016**, *12*, 9666-9673.

[35] J. A. Burns, J. C. Butler, J. Moran, G. M. Whitesides, *J. Org. Chem.* **1991**, *56*, 2648-2650.

[36] M. T. W. Lee, A. Maruani, J. R. Baker, S. Caddick, V. Chudasama, *Chem. Sci.* **2016**, *7*, 799-802.

[37] J. Düring, A. Hölzer, U. Kolb, R. Branscheid, F. Gröhn, *Angew. Chem. Int. Ed.* **2013**, *52*, 8742-8745.

[38] M. Karg, I. Pastoriza-Santos, J. Pérez-Juste, T. Hellweg, L. M. Liz-Marzán, *Small* **2007**, *3*, 1222-1229.

[39] H. Häkkinen, *Nat. Chem.* **2012**, *4*, 443-455.

[40] N. A. Alcantar, E. S. Aydil, J. N. Israelachvili, *J. Biomed. Mater. Res.* **2000**, *51*, 343-351.

[41] R. Gref, A. Domb, P. Quellec, T. Blunk, R. H. Müller, J. M. Verbavatz, R. Langer, *Adv. Drug Deliv. Rev.* **2012**, *64*, 316-326.

[42] K. Setoura, D. Werner, S. Hashimoto, *J. Phys. Chem. C* **2012**, *116*, 15458-15466.

[43] P. Grua, H. Bercegol, *Proc. SPIE* **2000**, *4347*, 579-587.

[44] R. Thomas, S. Z. F. Phua, S. Sreejith, Y. Zhao, C. B. Soh, *Nanoscale* **2017**, *9*, 15356-15361.

[45] R. Thomas, S. Sreejith, H. Joshi, S. Pedireddy, M. C. Stuparu, Y. Zhao, S. C. Boon, *J. Phys. Chem. C* **2016**, *120*, 11230-11236.

[46] E. Dulkeith, M. Ringler, T. A. Klar, J. Feldmann, A. M. Javier, W. J. Parak, *Nano Lett.* **2005**, *5*, 585-589.

[47] M. Brust, M. Walker, D. Bethell, D. J. Schiffrin, R. Whyman, *J. Chem. Soc. Chem. Commun.* **1994**, 801-802.

[48] Y. Jiao, J. Yin, H. He, X. Peng, Q. Gao, C. Duan, *J. Am. Chem. Soc.* **2018**, *140*, 5882-5885.

[49] K. Shiraishi, M. Yokoyama, *Sci. Technol. Adv. Mater.* **2019**, 20, 324-336.

[50] A. J. Tavares, W. Poon, Y. N. Zhang, Q. Dai, R. Besla,D. Ding, B. Ouyang, A. Li, J. Chen, G. Zheng, C. Robbins, W. C. W. Chan, C. J. Murphy, *Proc. Natl. Acad. Sci. U. S. A.* **2017**, *114*, 10871-10880.

[51] C. A. Simpson, A. C. Agrawal, A. Balinski, K. M. Harkness, D. E. Cliffel, *ACS Nano* **2011**, *5*, 3577-3584.

[52] N. Hoshyar, S. Gray, H. Han, G. Bao, *Nanomedicine* **2016**, *11*, 673-692.

[53] Y. Dou, Y. Guo, X. Li, X. Li, S. Wang, L. Wang, G. Lv, X. Zhang, H. Wang, X. Gong, J. Chang, *ACS Nano* **2016**, *10*, 2536-2548.

[54] J. Zhang, C. Li, X. Zhang, S. Huo, S. Jin, F. F. An, X. Wang, X. Xue, C. I. Okeke, G. Duan, F. Guo, X. Zhang, J. Hao, P. C. Wang, J. Zhang, X. J. Liang, *Biomaterials* **2015**, *42*, 103-111.

[55] J. Kim, P. Chhour, J. Hsu, H. I. Litt, V. A. Ferrari, R. Popovtzer, D. P. Cormode, *Bioconjugate Chem.* **2017**, *28*, 1581-1597.

[56] H. Lusic, M. W. Grinstaff, *Chem. Rev.* **2013**, *113*, 1641-1666.

[57] J. F. Hainfeld, D. N. Slatkin, T. M. Focella, H. M. Smilowitz, *Br. J. Radiol.* **2006**, *79*, 248-253.

[58] D. Xi, S. Dong, X. Meng, Q. Lu, L. Meng, J. Ye, *RSC Adv.* **2012**, *2*, 12515-12524.

[59] A. Jakhmola, N. Anton, T. F. Vandamme, *Adv. Healthcare Mater.* **2012**, *1*, 413-431.

[60] R. Prasad, S. B. Agawane, D. S. Chauhan, R. Srivastava, K. Selvaraj, *Bioconjugate Chem.* **2018**, *29*, 4012-4019.

[61] T. Reuveni, M. Motiei, Z. Romman, A. Popovtzer, R. Popovtzer, *Int. J. Nanomedicine* **2011**, *6*, 2859-2864.

[62] Q. Yin, F. Y. Yap, L. Yin, L. Ma, Q. Zhou, L. W. Dobrucki, T. M. Fan, R. C. Gaba, J. Cheng, *J. Am. Chem. Soc.* **2013**, *135*, 13620-13623.

[63] C. Ju, R. Mo, J. Xue, L. Zhang, Z. Zhao, L. Xue, Q. Ping, C. Zhang, *Angew. Chem. Int. Ed.* **2014**, *53*, 6253-6258.

[64] E. A. Sykes, Q. Dai, C. D. Sarsons, J. Chen, J. V. Rocheleau, D. M. Hwang, G. Zheng, D. T. Cramb, K. D. Rinker, W. C. W. Chan, *Proc. Natl. Acad. Sci. U. S. A.* **2016**, *113*, 1142-1151.

[65] J. Manson, D. Kumar, B. J. Meenan, D. Dixon, *Gold Bull.* **2011**, *44*, 99-105.

[66] P. Rajendra, J. Nishant, G. Mahadeo, S. C. Deepak, S. Y. Amit, C. João, S. T. Avnesh, K. Gopal, S. Rohit, *Commun. Biol*. **2020**, *3*, 284.

Table of Contents Graphic

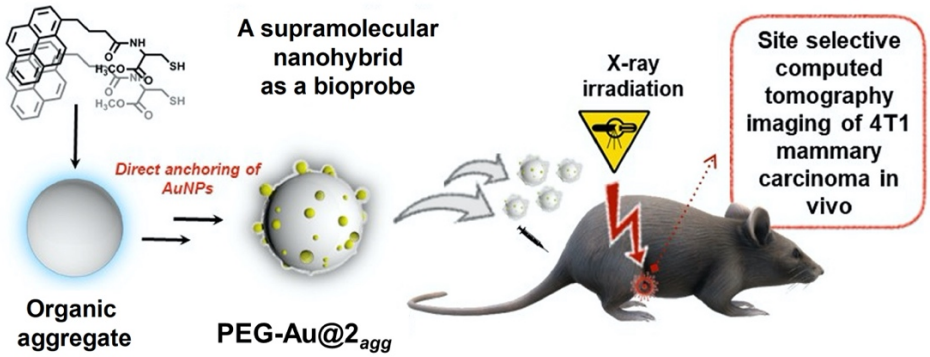

An organic-inorganic nanoprobe is developed using direct anchoring of gold nanoparticles over the self-assembled thiol-tailed pyrene nanostructures via Au-S interactions, demonstrating an efficient contrast agent for X-ray computed tomography imaging.